CrossMark

RESEARCH ARTICLE

Translational and rotational dynamics of a large buoyant sphere in turbulence

Varghese Mathai[1] · Matthijs W. M. Neut[1] · Erwin P. van der Poel[1] · Chao Sun[1,2]

Abstract We report experimental measurements of the translational and rotational dynamics of a large buoyant sphere in isotropic turbulence. We introduce an efficient method to simultaneously determine the position and (absolute) orientation of a spherical body from visual observation. The method employs a minimization algorithm to obtain the orientation from the 2D projection of a specific pattern drawn onto the surface of the sphere. This has the advantages that it does not require a database of reference images, is easily scalable using parallel processing, and enables accurate absolute orientation reference. Analysis of the sphere's translational dynamics reveals clear differences between the streamwise and transverse directions. The translational autocorrelations and PDFs provide evidence for periodicity in the particle's dynamics even under turbulent conditions. The angular autocorrelations show weak periodicity. The angular accelerations exhibit wide tails, however without a directional dependence.

✉ Varghese Mathai
v.mathai@utwente.nl

Chao Sun
chaosun@tsinghua.edu.cn

[1] Physics of Fluids Group, Mesa+ Institute, and J. M. Burgers Centre for Fluid Dynamics, University of Twente, 7500, AE, Enschede, The Netherlands

[2] Center for Combustion Energy and Department of Thermal Engineering, Tsinghua University, Beijing 100084, China

1 Introduction

Particles suspensions in turbulent flows can be found in a wide range of natural and industrial settings. The behavior of these particles depends on several parameters including their size and density ratio, the particle Reynolds number, the particle Stokes number and the Taylor Reynolds number of the carrier turbulent flow. Understanding how the dynamics of particles is influenced by these parameters is crucial to make predictions on global phenomena of interest such as pollutant transport, cloud formation, and mixing in industrial processes (Toschi and Bodenschatz 2009).

In many natural settings, particles can have a large size, and their density can be different from the carrier fluid. Theoretical studies often model such objects as passive, finite-sized particles advected by the flow (Maxey and Riley 1983; Calzavarini et al. 2009; Biferale et al. 2005). These are applicable in the limit of vanishing particle and shear Reynolds numbers. However, in most practical situations, the density mismatch of particles with the fluid results in finite drift velocities, which leads to finite particle Reynolds numbers (Jimenez 1997; MacKenzie and Leggett 1993; Skyllingstad et al. 1999; Mathai et al. 2015 etc). In such situations, particle dynamics can be strongly influenced by the unsteady wake-induced forces. For instance, a large buoyant sphere freely rising through quiescent fluid displays rich variability in translational dynamics (Ern et al. 2012; Horowitz and Williamson 2008, 2010). The forcing responsible for such varied dynamics is linked to the vorticity shed in the wake of the particle (Achenbach 1974; Govardhan and Williamson 2005). Since these forces may not act along the geometric center of the particle, it is possible that these could as well induce torques on the body. Little is known about the resulting translational and

rotational dynamics, particularly for the case of buoyant particles in turbulence, which motivates us to develop a reliable measurement technique for studying these issues.

In three dimensions, an object's location and orientation can be fully described by six independent variables. Many physical experiments rely on image analysis to obtain these parameters from experimental data (Bovik 2010; Meyer et al. 2013). Most of these systems capture translation and retrieve orientation from relative motion of translating nodes (Klein et al. 2013). In the more elementary forms, the translation of nodes could be used to determine the velocities of the particles. However, these methods were not accurate enough when higher derivatives of orientation were to be determined. Zimmermann et al. (2011b) introduced a method based on the identification of possible orientation candidates at each time step using projections of a pattern painted on the surface of a sphere. They found surprisingly intermittent behavior in the acceleration statistics of a neutrally buoyant sphere of diameter of the order of the integral scale.

In the present work, we introduce buoyancy to the problem of spherical particle dynamics in turbulence. We recover the translation and rotation as a function of time. The core of the method, which is to compare experimental images to synthetic ones, is the same as proposed by Zimmermann et al. (2011b). The novelty here lies in the way the pattern is generated (both physically on the surface of the particle and numerically for the comparison with actual images to match the orientation). Hence, the synthetic images for any given orientation are analytically known and do not need to be determined from static images. Furthermore, the method is easily scalable using parallel processing, which enables an accurate absolute orientation reference. These aspects are elucidated in Sect. 3. In addition, we describe a smoothing spline-based roughness-limiting technique that enables accurate representation of the higher derivatives of experimental data. Finally, in Sect. 5, we present the main results of our investigation on translational and rotational dynamics.

2 Experimental setup

The experiments were conducted in the Twente Water Tunnel facility (TWT), designed to study particle-laden flows (see Fig. 1 and Rensen et al. 2005). The measurement section has dimensions $0.45 \times 0.45 \times 2$ m^3, with three glass walls providing optical access to perform particle tracking experiments. The setup houses an active grid above the measurement section, consisting of 24 independently rotating motors, which produce nearly homogeneous and isotropic turbulence with Re$_\lambda$ up to 300 in the downstream section of the water tunnel. The flow in the measurement

section was characterized using a cylindrical hot film probe (Dantec 55R11) by following the same methodology as reported in Mercado et al. (2012). The experiment reported here was performed at Re$_\lambda \approx 300$. The dissipation rate $\epsilon = 505 \times 10^{-6}$ m^2/s^3, and the dissipation length and timescales were approximately 211 μm and 44 ms, respectively. The sphere used in the study has a diameter, $d_p = 25$ mm, with an effective mass ratio, $m^* \approx 0.82$, where m^* is the ratio of mass of sphere to mass of the sphere's volume of water (see Govardhan and Williamson 2005). The mass ratio was chosen such that the mean rise velocity of the sphere matched the mean downward flow velocity in the measurement section. This was necessary for obtaining sufficiently long sphere trajectories for well-converged Lagrangian statistics. The spheres were designed as spherical shells with the MP300 resin, with a bulk density ≈ 1089 kg/m^3. The angular inertia of the sphere was comparable to that of a homogeneous sphere of water, as was the case in the study by Zimmermann et al. (2011b). The spherical shells were made using a 3D printing technique, and the surface roughness was within 50 microns. The printing resolution depended on two factors. First, the resolution of the 3D printer used for making the stencil. In the present case, we could produce complex stencil designs with dimensions as small as a millimeter on a 25-mm
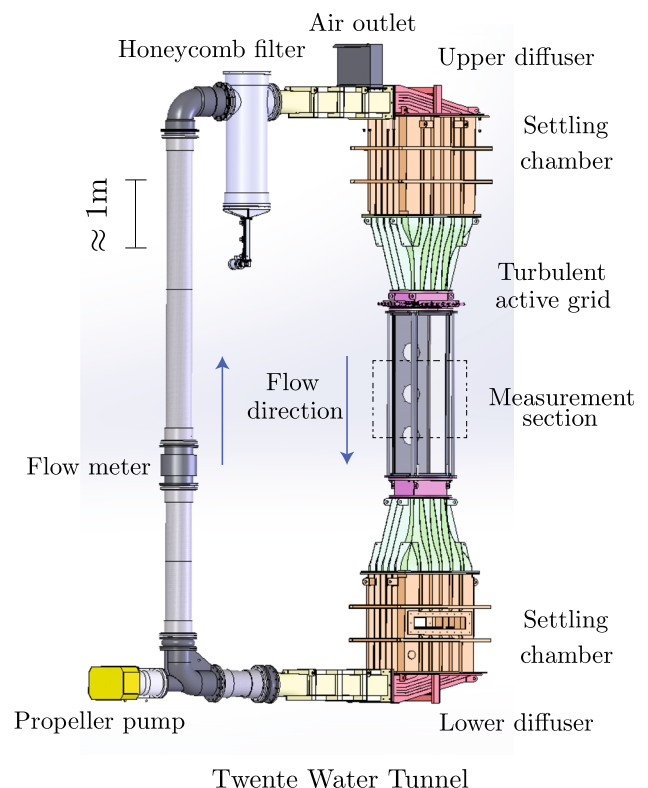
Fig. 1 Sketch of the Twente Water Tunnel facility used for the measurements reported in the present study

sphere. The second limiting factor was the painting procedure itself. Once the stencil was fixed on the sphere, the pattern had to be spray painted. Here again, it was practical to spray paint patterns of 2 mm smaller dimension.

The recordings were made with two Photron PCI-1024 high-speed cameras at 500 fps and megapixel resolution (see Fig. 2a, b). The cameras were positioned at a 90° angle between them and focused at the center of the test section on a 150×150 mm^2 area, which resulted in a spatial resolution of 150 μm/pixel. The images showed that perspective effects were negligible. This was done by placing a sphere of known orientation at the corners of the field of view. The retrieved orientation varied <3°. The measurement volume was lit by eight 20-W LED lamps from the sides. The flow velocity was tuned to ensure that the spheres stayed in the viewing window for considerable duration.

3 Method

The position and orientation of the sphere are determined using image analysis methods. The background was painted gray for contrast between the black-and-white pattern on the sphere. The sphere is separated from the background by subtracting the absolute difference in intensity from the background image. Subtracting the absolute difference yields a full dark circle with a brighter background. The sphere is then detected using the Circular Hough transform (CHT) technique, and the centroid of the detected circle gives its position. The accuracy of CHT varied with angle of view. Therefore, choosing a good pattern is one of the most important steps. We found that a pattern that contained almost equal fraction of dark and bright areas for most angles of view improved the circle detection accuracy. Additionally, we used the outputs from previous frames to improve and speed up the detection process. The CHT also returns the detected circle diameter D_c in pixels from the image. Since the sphere diameter (25 mm) is known, we use a calibration ($25/D_c$) mm/pixels for the recorded images. This ensures a correction for the minor magnification changes due to the sphere moving forward or backward in the measurement section.

There are several approaches to obtaining the three-dimensional trajectory of a particle. One approach is to reconstruct the spatial positions using multiple cameras (Ouellette et al. 2006). Precise spatial reconstruction is needed when there are multiple particles in the image and identifying and separating particles can be a challenge. In the present work, there are only a few particles in the measurement volume. We use a different method using two orthogonal cameras to obtain the three-dimensional trajectory. The camera arrangement is such that the

magnification and field of view are comparable between the two cameras. The camera field of view covered the full width of the water tunnel. We first obtain two-dimensional trajectories of particles from both cameras. The redundant data corresponding to the vertical motion for two cameras is used to compare individual trajectories. In order to avoid ambiguities, we cross-correlate the vertical acceleration time series from the two cameras. A match is said to be found when the cross-correlation of two acceleration time series yields a coefficient greater than 98 %, even for long trajectories such as the one shown in Fig. 2b. This yields a simple yet robust three-dimensional track of the particles without needing to resort to complex spatial reconstruction algorithms.

Obtaining the rotation of the sphere is a more complex task compared to position tracking. Hence, the remainder of this section will be used to describe the method that is used to obtain the rotation. The method to determine the
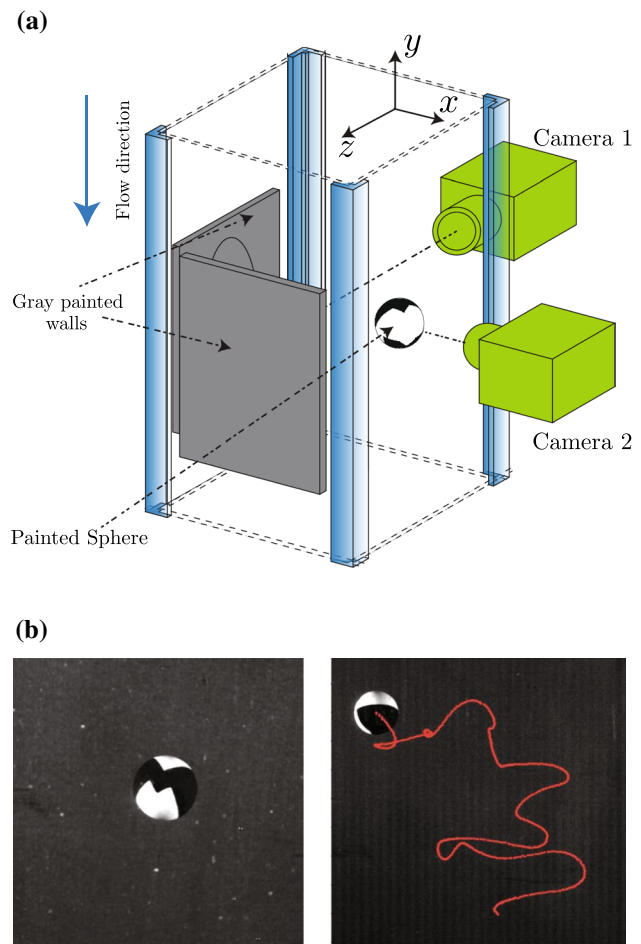
Fig. 2 a Measurement section of the Twente Water Tunnel with orthogonal camera experimental arrangement. A painted sphere is shown, which is viewed by both cameras. **b** The sphere and its trajectory as recorded by one of the cameras

rotation can be divided into four parts. Initially, a suitable Boolean surface pattern is created. This pattern can be described as a piecewise constant analytic function $F(\theta, \phi)$ such that, given a coordinate on the surface of the sphere, the function returns either a zero or a one depending on the color of its corresponding infinitesimally small surface element. Here, θ and ϕ are the azimuthal and the polar angles, respectively, and $F(\theta, \phi)$ is radius independent. Second, the pattern is drawn onto a physical sphere. This is realized using a 3D-printed painting stencil and an airbrush system. It is imperative that $F(\theta, \phi)$ is painted as accurate as possible to decrease the introduced error in this step. Third, a synthetic 2D image is constructed from a projection of the surface of the sphere onto a plane. The synthetic image for any given orientation is analytically known and does not need to be determined from static images. The projection is a function of the angle of rotation of the sphere and can be conceptually understood as the analog of the projection of the physical sphere on the recording camera. Finally, the rotated and projected synthetic pattern is compared to an image of the physical sphere. The minimizing function can take different forms. For instance, a cross-correlation function between the synthetic pattern and the camera image could be used to find the best match. Alternately, a suitable cost function may be used to search for a match. Here, we use a cost function, defined as the sum of the absolute difference between the binarized image pixels and the corresponding pixels in the synthetic image. The orientation for which this comparison yields the best match is then determined using a Nelder–Mead minimization algorithm. These steps are illustrated in a flowchart in Fig. 3. The Fortran90 code and the stl-file of the stencil used for painting the spheres have been included as supplemental material (Fig. 4).

The choice of painted pattern is an important step in the method of orientation detection. A necessary condition is that the projection of $F(\theta, \phi)$ onto a plane must be unique for each orientation of the sphere. Additionally, it is desirable that the pattern contains a minimum of edges and corners. The latter criterion is essential for fast convergence of the algorithm to the global minimum. Here, we use the axis-angle method to describe the orientation considering its straightforward and singularity-free definition. It allows for smooth and continuous rotation from any orientation including around the Euler angle singularities as it does not suffer from gimbal lock problems.

The pattern $F(\theta, \phi)$ represents a simply connected region, even then, some local minima may still arise due to the two-tone color limit. When the orientation is unknown, for instance in the first frame of a movie, a comparison of several initial orientation estimates solves this local minima problem. This yields the global minima. However, every initial estimate reduces the performance. Fortunately, given
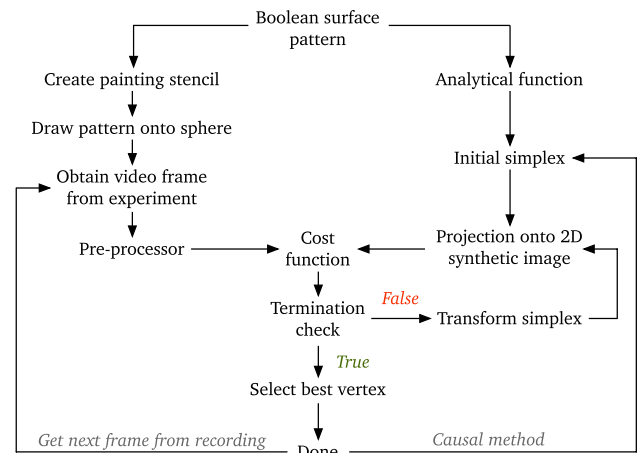

Fig. 3 Orientation detection method flowchart
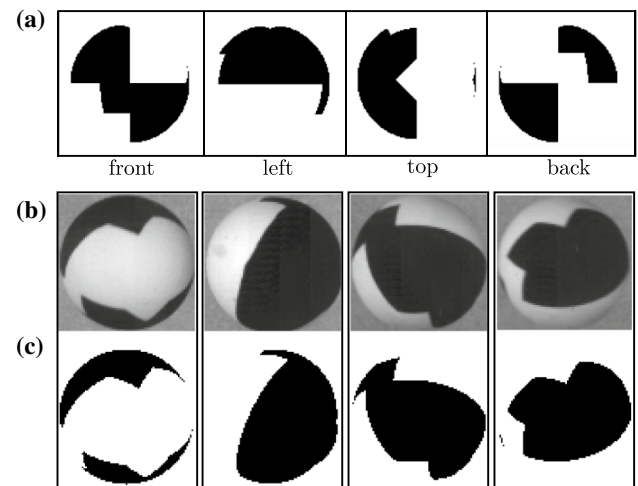

Fig. 4 **a** Several viewpoints of the synthetic pattern. Here, the synthetic projection is defined in the axis-angle convention as *front*: $\rho = (1, 0, 0, 0°)$, *left*: $\rho = (0, 0, 1, -90°)$, *top*: $\rho = (0, 1, 0, -90°)$ and *back*: $\rho = (0, 0, 1, 180°)$. **b** Experimental images of the sphere with the painted pattern for arbitrary orientations. **c** Synthetic image equivalents as found by the orientation detection program corresponding to the experimental images in **b**

a sufficiently high ratio of frame rate over rotation rate, any frame in a sequence may use the outcome of the previous frame as initial estimate, reducing the number of initial estimates required to just one. This *causal* method is the preferred method for analyzing large sequential datasets. The computational performance of the method is approximately 30 frames per second on a contemporary computer, suggesting that processing of large datasets is straightforward.

To determine the numerical accuracy of the method, several sets of 1024 projections are created using pseudo-random generated orientations. These synthetic images are used as input to our algorithm. A probability density function of the difference between the actual orientation and the orientation
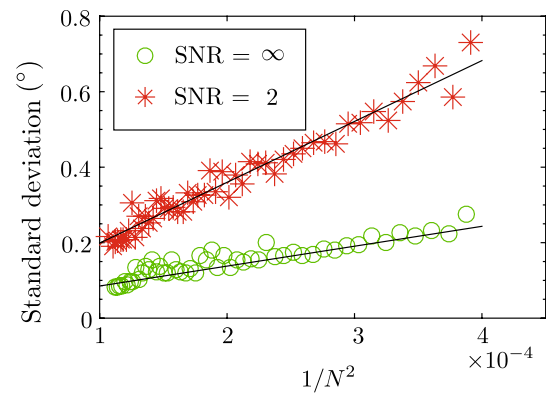
(a)

(b)
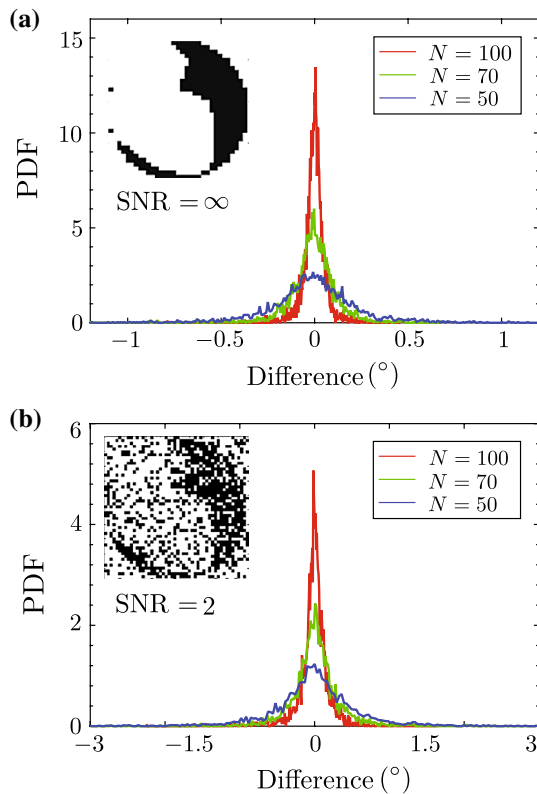
Fig. 5 PDFs of the difference between actual orientation and orientation as found by the orientation detection method for different signal-to-noise ratios (SNR). **a** SNR $= \infty$ and **b** SNR $= 2$. Here N is the width of the sphere in the image in pixels. N takes on values 50, 70 ad 100 in the three cases shown. With increasing resolution N, the width of the PDF decreases

Fig. 6 Numerical error scaling R^2 of linear fits are 0.87 and 0.96 for the SNR $= \infty$ and SNR $= 2$, respectively

as found by the algorithm is shown in Fig. 5a, b, and the corresponding scaling of the standard deviation as function of the image width N (in pixels) is shown in Fig. 6. The standard deviation of accuracy scales as $\mathcal{O}(N^{-2})$, and assuming a Gaussian error distribution, this means that <1 % of the measured data showed an error larger than 1° for $N \geq 50$. Also, Fig. 6 shows that noise decreases the accuracy to some extent but does not affect the reliability of the algorithm. In the experiment, most image artifacts arise due to shadows and glare, which may be reduced by using diffuse light sources and a matte-paint finish on the surface of the sphere.

The axis-angle output, $\rho \equiv (k_x, k_y, k_z, \alpha)$, is defined with respect to a reference orientation in the camera coordinate system (see leftmost image in Fig. 4a). A typical output obtained from a buoyant sphere in a turbulent flow is given in Fig. 9a. This output has little physical significance. Quantities of greater relevance to a rotating sphere are its rotational kinetic energy $I\omega^2$ and the net torque exerted on it by the surrounding fluid $I\alpha$, where I is the moment of inertia of the sphere, and ω and α are the angular velocity and acceleration, respectively. We adopt the following

approach to compute ω and α in the laboratory coordinate system. Firstly, a high framing rate is used for accurate estimation of the time derivatives. In the present case, a frame rate of 500 fps ensures about 30 recordings in one Kolmogorov time. Therefore, within the inter-frame time interval $\Delta t = 1/500$ s, the particle's angular velocity may be assumed constant.

According to Euler's theorem, the angular velocity is linked to the inter-frame axis-angle, $\rho_\Delta \equiv (k_{\Delta x}, k_{\Delta y}, k_{\Delta z}, \Delta \alpha)$, by the relation

$$\omega(t) = \frac{\Delta \alpha}{\Delta t} \left(k_{\Delta x} \hat{i} + k_{\Delta y} \hat{j} + k_{\Delta z} \hat{k} \right). \tag{1}$$

Now ρ_Δ may be obtained from the reference orientation-based axis-angle output (ρ) through a few transformations. Firstly, the axis-angle output is converted to rotation matrix using Rodrigues formula. Let $[R_{0,i}]$ and $[R_{0,(i+1)}]$ represent the rotation matrices corresponding to rotations from the reference orientation to the orientations in ith and $(i + 1)$th images, respectively. Then $[R_{0,i}] \times [R_{i,(i+1)}] = [R_{0,(i+1)}]$ and consequently, the inter-frame rotation matrix $[R_{i,(i+1)}] = [R_{0,i}]^T \times [R_{0,(i+1)}]$. This follows from the identity that $[R]^{-1} = [R]^T$ for rotation matrices. From $[R_{i,(i+1)}]$, $\rho_\Delta \equiv \rho_{i,(i+1)}$ may be obtained, and Eq. 1 gives the angular velocity $\omega(t)$ in the laboratory coordinate system.

The accuracy of the detection in a real experiment needs to be verified by other methods. We use a two-camera arrangement for this. If the orientations determined by the two cameras are comparable, then the method can be regarded accurate. Figure 9b shows the three orientation angles obtained from Camera 1 for a long particle trajectory. The same sphere was captured by Camera 2, which was placed at a 90° angle with Camera 1. The difference in orientation prediction is plotted in Fig. 9c. The maximum deviation is within 2.5°. These differences are due to experimental noise and may be filtered out in the data smoothing step, to be explained in the following section.

4 Evaluating higher derivatives from experimental data

Evaluating the forces and torques is an important step in understanding any dynamical system. One way to do this is by using accelerometers. However, this may not always be convenient since a direct measurement of acceleration usually requires attaching devices to the body. Moreover, the method is intrusive in nature and often leads to variations in the mass and center of gravity of the system (Zimmermann et al. 2013). In such situations, it may be suitable to numerically compute the acceleration from the second derivative of position of the body. This approach is the basis of our present study, where we determine both the position and orientation of a large buoyant sphere in turbulence using recordings from a high-speed camera.

Estimating the derivatives from experimentally determined position and orientation data is a nontrivial task. The difficulty arises because data obtained from experiments will have inherent noise due to measurement uncertainties. Historically, there have been two popular methods for smoothing particle trajectories in turbulent flows. One method involves fitting parts of the particle trajectory to a polynomial of second order or higher. Voth et al. (2002) used a second-order polynomial, Lüthi et al. (2005) and Mercado et al. (2012) used a third-order polynomial. Other researchers have used a Gaussian kernel for smoothing (Mordant et al. 2004; Volk et al. 2011). Both the mentioned methods employ piecewise discontinuous fitting of analytical functions to smooth out the noise. The effectiveness of these methods in filtering out the experimental noise depends on the fitting parameters chosen. In spite of the extensive literature on smoothing methods, there still prevails a general lack of consensus on the method of finding the optimal fitting parameter. Existing guidelines for the choice of the fitting parameters, such as those suggested by Mordant et al. (2004), require knowledge of the smallest timescales in the flow a priori, and therefore are likely to introduce a bias into the analysis.

In this paper, we explore an alternate method using smoothing splines to filter out the experimental noise. The method is based roughly on the work by Epps (2010). While this was originally used to estimate the translational accelerations experienced by a water-entering object (Truscott et al. 2012; Truscott 2009), the method may be applied to particle trajectories in turbulence. Consider a general set of experimental data $y(t)$ acquired at high temporal resolution. We use a smoothing spline-based roughness-limiting method to reduce the experimental noise in the data for obtaining higher derivatives. The function *spaps* in Matlab is defined by two fitting parameters: the order of the smoothing spline and the error tolerance,

$E(s) = \int_{t_1}^{t_N} |y(t) - s(t)|^2 dt$. We use a *quintic* smoothing spline, which ensures that the second derivatives are properly represented. This leaves us with one fitting parameter, the error tolerance. We use a roughness estimate, $R(s) = \int_{t_1}^{t_N} |\frac{d^3 s}{dt^3}|^2 dt$, to scan for the most suitable fit to the experimental data. This is based on the assumption that the true function does not have very large changes in acceleration, which typically are due to noise in the data. In Fig. 7, we demonstrate the step to determine the optimal fit from experimental data. Increasing the error tolerance beyond E_{crit} does not reduce the roughness of the curve. For error tolerances below E_{crit}, the roughness of the fits is increased significantly, indicating that the noise contained in the data is not properly removed. Therefore, the fit corresponding to the kink can be thought to best represent the true curve.

We test the sensitivity of the velocity and acceleration to the choice of the spline. For this, we use a sample analytical function defined as a combination of sine functions, $y = a \sin x + b \sin 2x + c \sin 4x + d \sin 10x$, where a, b, c and d were generated randomly in the [0 1] range. We introduce random noise to the signal with signal-to-noise-ratio ≈ 4. The true function and noisy input are shown in Fig. 8a. In Fig. 8c–h, we compare the velocity and acceleration estimates for critical (E_{crit}), subcritical (E_1) and super-critical (E_2) error tolerances. The subcritical error tolerance (Fig. 8f) yields very high accelerations, while the super-critical error tolerance over-smoothes the curve (Fig. 8h). Clearly, the acceleration estimate for critical error tolerance was obtained without prior knowledge of the timescales of the flow or the particle, and it compares fairly well with the analytical second derivative.

Another interesting feature of the present method is that the kink (Figs. 7, 8b) flattens out for experimental data with low signal-to-noise-ratios. Thus, the method also serves
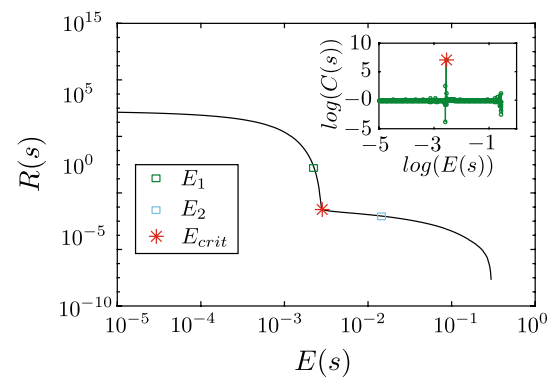

Fig. 7 Roughness versus error frontier for a family of candidate smoothing splines. The kink marks the critical error tolerance of the optimal smoothing spline. *Inset* shows $\log(C(s))$ versus $\log(E(s))$. The optimal fit corresponds to the maximum curvature point indicated by the *red star symbol*

Fig. 8 **a** Analytical function and the noisy data with SNR ≈ 4. *Inset* shows a zoom-in of the noisy data. **b** Roughness versus error frontier for the noisy data. First and second derivatives (velocity and acceleration) estimated for **c** and **d** $E = E_{crit}$, **e** and **f** $E = E_1$, and **g** and **h** $E = E_2$. $E = E_{crit}$ gives an accurate estimate of even the second derivative, except at the endpoints
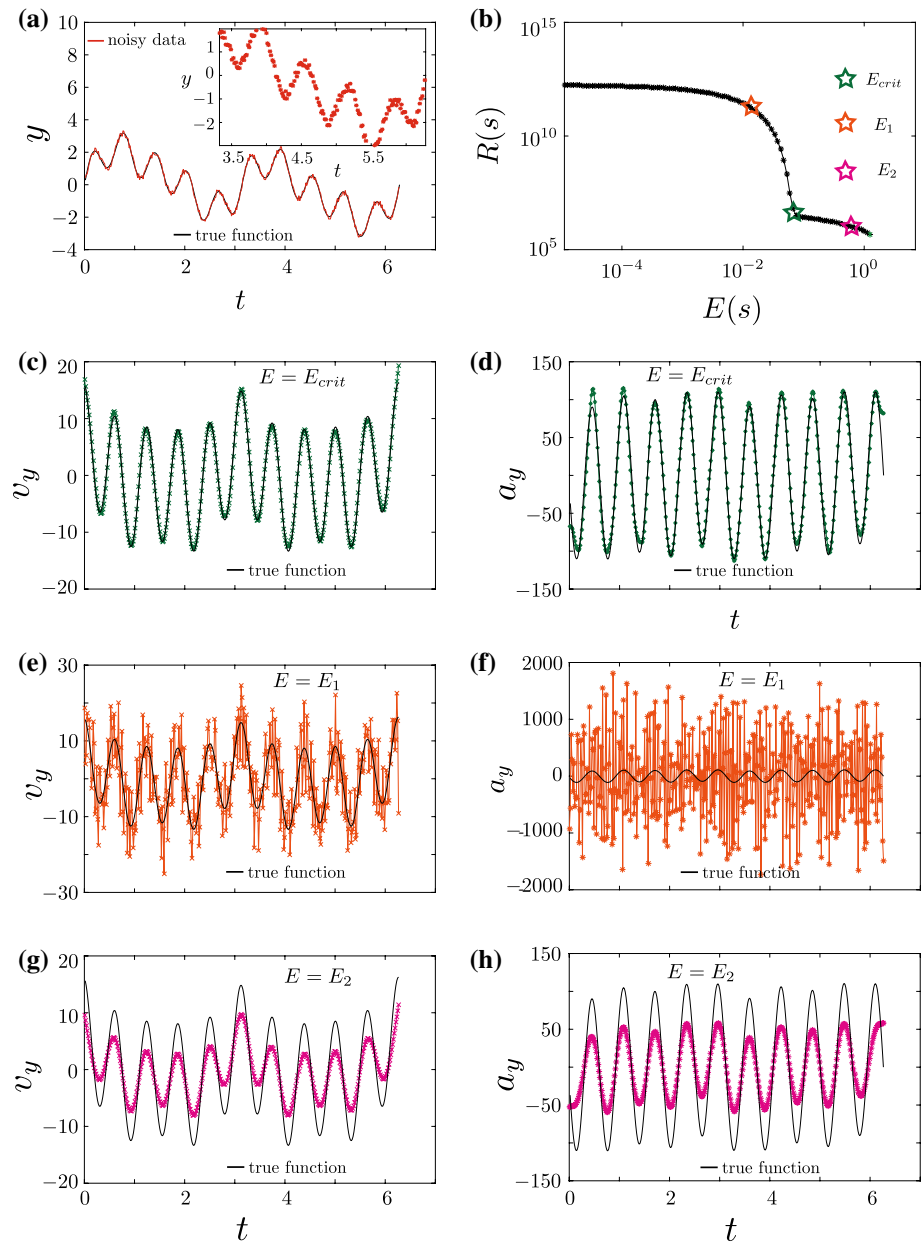

Fig. 9 **a** Axis-angle output obtained for a long trajectory of a buoyant sphere in a turbulent flow. **b** Orientation $(\theta_x, \theta_y, \theta_z)$ obtained from Camera 1. **c** Absolute difference between independent orientation measurements from Camera 1 and Camera 2. The maximum deviation is within 2.5°. Mean of the difference is within 0.2°
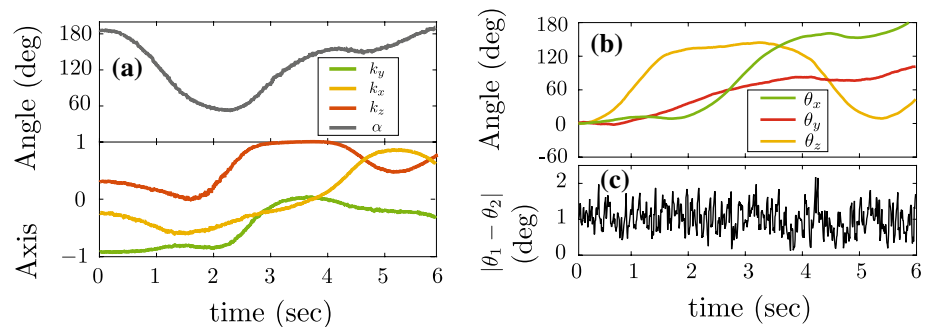
as a check for the quality of data, which can be difficult to estimate for standard smoothing methods. Alternately, the spline fit guess for the particle acceleration from a few representative tracks could be used to determine the optimal parameters for Gaussian Kernel smoothing (Ouellette 2006). This can speed up the fitting process when sampling large datasets, while ensuring that the fitting windows are properly chosen (Fig. 9).

5 Results and discussion

We present results on the translational and rotational motion of a large buoyant sphere in nearly homogeneous and isotropic turbulence. We first address the question of how the particle's translational velocity and acceleration decorrelate in time. In Fig. 10a, we plot the Lagrangian autocorrelation function for the horizontal (x and z directions) velocity and accelerations. The particle response scale is fairly well predicted from the relation $\tau_v = d_p/(\text{St} \times U_r)$, where St—Strouhal number ≈ 0.2, and U_r is the measured mean rise velocity relative to the flow. Interestingly, both velocity and acceleration decorrelate in the same time ~ 0.5 s, and
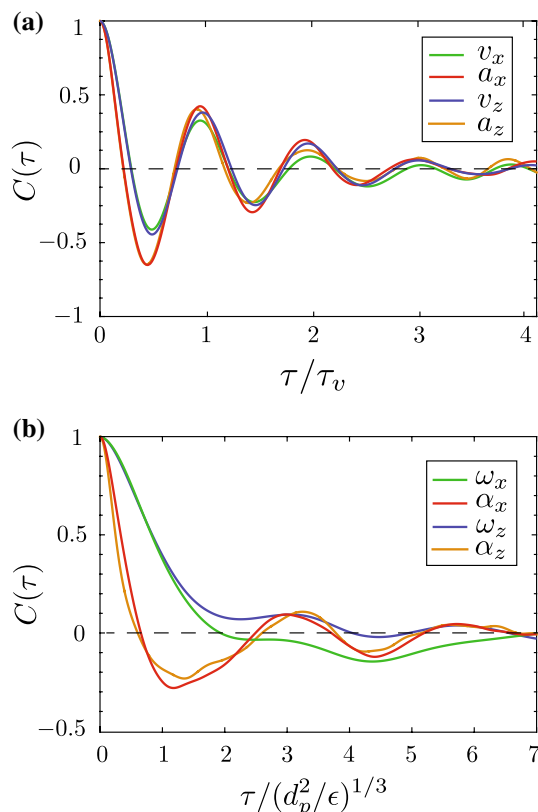
Fig. 10 a Lagrangian autocorrelation function of **a** translational and **b** rotational velocities and accelerations for the buoyant sphere in turbulence

they both display periodicity. This decorrelation behavior is fundamentally different from that of a passive finite-size particle in turbulence, for which the acceleration decorrelates in much shorter time than the velocity (Ishihara et al. 2009). Therefore, in the present case, the dominant velocities and accelerations originate from vortices with the same timescale.

Figure 10b shows the angular velocities and accelerations in the horizontal direction. The time axis is normalized with the particle-sized eddy timescale, $\tau_d = (d_p^2/\epsilon)^{1/3} \sim 1$ s. The angular acceleration crosses the first minima in approximately 1 τ_d, which is four times longer compared to the minima crossing time for translational acceleration. The angular velocity components decorrelate even slower than the angular acceleration, and they show only a weak periodicity. The angular velocities and translational accelerations are weakly correlated, with a correlation coefficient ≈ 0.05. Surprisingly, we do not find any preferential orientation of the angular velocity vector with the translational acceleration vector, as found by Zimmermann et al. (2011a). Therefore, in the present case, particle rotation does not appear synchronized with its translational motion, and we find no strong evidence suggesting a lift force. More detailed studies are to be conducted to gain further insights into the underlying physics. In future, we also aim to look into the flow structure around the sphere along with its motion.

In Fig. 11a, b, we show the probability density functions (PDFs) of the horizontal and vertical components of the velocity and acceleration. The horizontal velocity PDF shows a symmetric flat-head distribution with sub-Gaussian tails. The behavior is notably different from the nearly Gaussian velocity PDFs found for neutrally buoyant particles (Mercado et al. 2012). The flat top of the PDF may be explained from a typical time series of velocity of the sphere. We observe that the particle undergoes repeated cyclic motions, weakly disturbed by the carrier flow. The velocities in these cycles lie in the $\pm 1.5 \langle a^2 \rangle^{1/2}$ range. More extreme accelerations are less frequent and contribute to the low probability tails of the PDFs. The horizontal acceleration PDF is Gaussian. The vertical velocity and accelerations have positively skewed distributions, clearly indicating a directional dependence. This strong anisotropy is not inherent in the carrier turbulent flow. The water tunnel flow was reported to be nearly isotropic in earlier studies (Mercado et al. 2012). Therefore, the anisotropy here is expected to originate from the up-down asymmetry set up by the vortex-shedding downstream of the sphere. The PDFs of the rotational quantities reveal a different story (Fig. 11c, d). Both horizontal and vertical angular velocities follow a nearly Gaussian distribution. The angular acceleration PDFs show symmetric distributions but with wide tails compared to the translational acceleration

Fig. 11 Velocity and acceleration PDFs in the **a** transverse and **b** streamwise directions for the buoyant sphere (25 mm diameter). Angular velocity and angular acceleration PDFs in the **c** transverse and **d** streamwise directions for the sphere. The PDFs have been shifted vertically for clarity of viewing
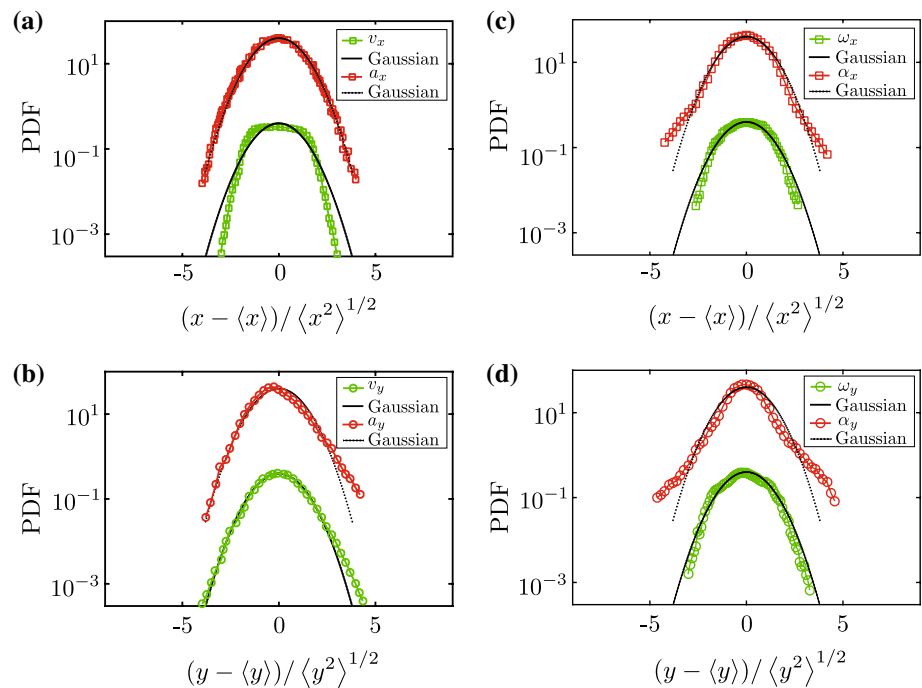
PDFs. It may be noted that Re_λ and particle size ratio $\Xi = d_p/\eta$ are comparable to the experiment of Zimmermann et al. (2011b). Thus, changing only the particle–fluid density ratio brings in these new effects, leading to observable differences in particle dynamics in turbulence. Future experiments will be aimed at tracking simultaneously the particle and the flow around it.

6 Conclusions

We have conducted experimental measurements of the dynamics of a large buoyant sphere in a turbulent flow and described the methods and procedures to track simultaneously its position and orientation. A fast, accurate and adaptable method that determines the absolute orientation of the sphere in 3D space is described and validated. The standard deviation of error for this method is approximately $0.2°$. Distortion using salt-and-pepper noise with $SNR = 2$ increases the standard deviation of error to $0.7°$, however without impacting the reliability of the method.

We followed the approach of using the experimentally determined data to calculate time derivatives (velocity and acceleration) of position and orientation. To this end, we employed a smoothing spline-based roughness-limiting technique, which enables an accurate estimation of higher derivatives. The method has the advantage that it yields an optimal fit that is continuous and differentiable.

Our results on the velocity and acceleration statistics reveal that buoyant spheres have very different dynamics from the well-explored class of neutrally buoyant particles in turbulence (Zimmermann et al. 2011b; Toschi and Bodenschatz 2009; Homann and Bec 2010). We detect the influence of trailing wake, resulting in periodicity in the Lagrangian autocorrelations and anisotropy in the translational dynamics. The rotational velocity and acceleration PDFs show wide tails, however without any observable skewness in the streamwise and transverse directions. The present measurements provide clues about how a buoyant particle interacts with a turbulent flow. The methods presented here open up a new direction in the exploration of particle dynamics in turbulence.

References

Achenbach E (1974) Vortex shedding from spheres. J Fluid Mech 62(02):209–221

Biferale L, Boffetta G, Celani A, Lanotte A, Toschi F (2005) Particle trapping in three-dimensional fully developed turbulence. Phys Fluids 17(2):021701 **(1994-present)**

Bovik AC (2010) Handbook of image and video processing. Academic Press, Cambridge

Calzavarini E, Volk R, Bourgoin M, Lévêque E, Pinton J-F, Toschi Federico (2009) Acceleration statistics of finite-sized particles in turbulent flow. J Fluid Mech 630:179–189

Epps BP (2010) An impulse framework for hydrodynamic force analysis: fish propulsion, water entry of spheres, and marine propellers. Ph.D. thesis, Massachusetts Institute of Technology

Ern P, Risso F, Fabre D, Magnaudet J (2012) Wake-induced oscillatory paths of bodies freely rising or falling in fluids. Annu Rev Fluid Mech 44:97–121

Govardhan RN, Williamson CHK (2005) Vortex-induced vibrations of a sphere. J Fluid Mech 531:11–47

Homann H, Bec J (2010) Finite-size effects in the dynamics of neutrally buoyant particles in turbulent flow. J Fluid Mech 651:81–91

Horowitz M, Williamson CHK (2008) Critical mass and a new periodic four-ring vortex wake mode for freely rising and falling spheres. Phys Fluids 20(10):101701 **(1994-present)**

Horowitz M, Williamson CHK (2010) The effect of Reynolds number on the dynamics and wakes of freely rising and falling spheres. J Fluid Mech 651:251–294

Ishihara T, Gotoh T, Kaneda Y (2009) Study of high-Reynolds number isotropic turbulence by direct numerical simulation. Annu Rev Fluid Mech 41:165–180

Jimenez J (1997) Oceanic turbulence at millimeter scales. Sci Mar 61:47–56

Klein S, Gibert M, Bérut A, Bodenschatz E (2013) Simultaneous 3d measurement of the translation and rotation of finite-size particles and the flow field in a fully developed turbulent water flow. Meas Sci Technol 24(2):024006

Lüthi B, Tsinober A, Kinzelbach W (2005) Lagrangian measurement of vorticity dynamics in turbulent flow. J Fluid Mech 528:87–118

MacKenzie BR, Leggett WC (1993) Wind-based models for estimating the dissipation rates of turbulent energy in aquatic environments: empirical comparisons. Mar Ecol Prog Ser 94:207–207

Mathai V, Prakash VN, Brons J, Sun C, Lohse D (2015) Wake-driven dynamics of finite-sized buoyant spheres in turbulence. Phys Rev Lett 115:124501

Maxey MR, Riley JJ (1983) Equation of motion for a small rigid sphere in a nonuniform flow. Phys Fluids 26(4):883–889 **(1958–1988)**

Mercado JM, Prakash VN, Tagawa Y, Sun C, Lohse Detlef et al (2012) Lagrangian statistics of light particles in turbulence. Phys Fluids 24(5):055106 **(1994-present)**

Meyer CR, Byron ML, Variano EA (2013) Rotational diffusion of particles in turbulence. Limnol Oceanogr Fluids Environ 3(1):89–102

Mordant N, Crawford AM, Bodenschatz E (2004) Experimental Lagrangian acceleration probability density function measurement. Phys D Nonlinear Phenom 193(1):245–251

Ouellette NT (2006) Probing the statistical structure of turbulence with measurements of tracer particle tracks. Cornell University, Ithaca

Ouellette NT, Xu H, Bodenschatz E (2006) A quantitative study of three-dimensional lagrangian particle tracking algorithms. Exp Fluids 40(2):301–313

Rensen J, Luther S, Lohse D (2005) The effect of bubbles on developed turbulence. J Fluid Mech 538:153–187

Skyllingstad ED, Smyth WD, Moum JN, Wijesekera H (1999) Upper-ocean turbulence during a westerly wind burst: a comparison of large-eddy simulation results and microstructure measurements. J Phys Oceanogr 29(1):5–28

Toschi F, Bodenschatz E (2009) Lagrangian properties of particles in turbulence. Annu Rev Fluid Mech 41:375–404

Truscott TT, Epps BP, Techet AH (2012) Unsteady forces on spheres during free-surface water entry. J Fluid Mech 704:173–210

Truscott TT (2009) Cavity dynamics of water entry for spheres and ballistic projectiles. Ph.D. thesis, Massachusetts Institute of Technology

Volk R, Calzavarini E, Leveque E, Pinton J-F (2011) Dynamics of inertial particles in a turbulent Von kármán flow. J Fluid Mech 668:223–235

Voth GA, la Porta A, Crawford AM, Alexander J, Bodenschatz E (2002) Measurement of particle accelerations in fully developed turbulence. J Fluid Mech 469:121–160

Zimmermann R, Gasteuil Y, Bourgoin M, Volk R, Pumir Alain, Pinton Jean-François (2011a) Rotational intermittency and turbulence induced lift experienced by large particles in a turbulent flow. Phys Rev Lett 106(15):154501

Zimmermann R, Gasteuil Y, Bourgoin M, Volk R, Pumir A, Pinton J-F et al (2011b) Tracking the dynamics of translation and absolute orientation of a sphere in a turbulent flow. Rev Sci Instrum 82(3):033906

Zimmermann R, Fiabane L, Gasteuil Y, Volk R, Pinton J-F (2013) Characterizing flows with an instrumented particle measuring Lagrangian accelerations. N J Phys 15(1):015018